On the Modification of Tides in a Seasonally Ice-Covered Sea

P. St-Laurent

Institut des Sciences de la Mer, Université du Québec à Rimouski, Rimouski, Québec, G5L 3A1, Canada

F. J. Saucier

Institut des Sciences de la Mer, Université du Québec à Rimouski, Rimouski, Québec, G5L 3A1, Canada

J.-F. Dumais

Institut des Sciences de la Mer, Université du Québec à Rimouski, Rimouski, Québec, G5L 3A1, Canada

Abstract.
New observations from eight moorings located in Foxe Basin, Hudson Strait, and Hudson Bay, are used to study the seasonal variability of the M_2 tide. Significant seasonal variations of the M_2 surface elevation are found in all these regions and at all seasons. The largest variations occur during winter while both elevation increase (Hudson Strait) and decrease (Hudson Bay, Foxe Basin) are observed. These variations are found recurrent at the stations where multiyear observations are available. Observations from a velocity profiler are consistent with a seasonal damping of the tides because of friction under ice. Numerical simulations with a sea ice-ocean coupled model and realistic forcing qualitatively reproduce most of the features of the observed variability. The simulations show that the winter M_2 variations are essentially caused by the under-ice friction, albeit with strong regional differences. Under-ice friction mostly occurs in a limited region (Foxe Basin) and can account for both increased and decreased M_2 elevations during winter.

1. Introduction

Seasonal changes in the characteristics of Arctic tidal waves have been reported as early as 1917 [*Zubov*, 1943]. The changes often consist in a decrease of tidal elevations during winter [*Zubov*, 1943; *Godin and Barber*, 1980; *Johnson and Kowalik*, 1986; *Murty*, 1985]. The lower elevations suggest a damping mechanism that dissipates tidal energy during winter. A potential damping mechanism is the friction produced at the interface between the ice and the ocean. For instance, *Sverdrup* [1927] described the near-surface shear layer formed by tidal currents underneath the ice.

Under-ice friction is particularly expected in the marginal seas that are characterized by significant tides and ice cover. The horizontal stress at the ice-ocean interface is often parameterized as the stress over the sea floor (a quadratic stress). Sea ice is seldom motionless so the stress is proportional to the relative velocity between ice and water [e.g., *Pease et al.*, 1983]. High levels of under-ice friction are expected during high ice concentration periods, i.e. when the ice cover is complete. The ice plates are then confined by shorelines and their mobility is significantly hampered. The relative velocity between the ice and the tidal current increases and the stress exerted over the tidal stream becomes significant.

Recent studies have shown that the interaction between ice and tides may play a significant role in the climate of ice-covered seas. The model study from *Polyakov and Martin* [2000] showed that tidal mixing helps in transporting heat to the sea surface and is important in the establishment and maintenance of a recurrent polynya in the Okhotsk Sea (see also observations from *Martin et al.* 2004). In a similar way, the parameterization of tides in the Arctic Ocean Model Intercomparison Project (AOMIP) led to a more realistic ventilation of ocean heat through atmosphere-ocean exchanges in tidal leads [*Holloway and Proshutinsky*, 2007]. *Heil et al.* [2008] also studied the drift and deformation of sea ice in the Weddell Sea using an array of drifting ice buoys. The sea ice velocity variance over the continent shelf was found to be dominated at semidiurnal frequencies by tides rather than inertial response. The variability of the sea-ice deformation was dominated by sub-daily processes (tides and inertial response) and low-frequency atmospheric changes played a secondary role.

While the importance of tides in the climate of ice-covered seas is investigated, the effect of ice upon tides remains elusive. Existing studies either show observed tidal variations alone [e.g., *Prinsenberg and Hamilton*, 2005] or model results without comparison with seasonal observations [*Kagan et al.*, 2008]. The precise role of the ice-ocean stress in the observed tidal variations is thus unclear. The Hudson Bay System (HBS), a shallow inland sea located in northern Canada (see Fig. 1), is an appropriate region to examine this process. The sea ice cover in HBS has a concentration c that seasonally fluctuates from $c \cong 0$ (generally ice-free conditions, around September) to $0.95 < c < 1$ (complete ice cover, around March). Significant seasonal variability of tides was reported in HBS by *Godin* [1986] and *Prinsenberg* [1988] who both suggested that the changes are related to the ice cover.

In this work, we re-examine the seasonal variations of the principal tidal wave (M_2) in the HBS using new observations and results from a sea ice-ocean coupled 3–D numerical model. The new observations extend the work from *Godin* [1986] and *Prinsenberg* [1988] by providing year-long coverage in Foxe Basin, Hudson Strait, and Hudson Bay. Section 2 describes the instruments and the numerical model used throughout the study. Section 3 shows the results from the observations. Significant seasonal changes in M_2 elevations are found throughout the Hudson Bay System. The numerical model is used in section 4 to examine the relationship between the under-ice friction and the seasonal variability of the M_2 tide. It is found that the winter variations of

0148-0227/11/$9.00

the M_2 tide are essentially caused by the under-ice friction, albeit with strong regional differences. Finally, these results are discussed in section 5.

2. Method

2.1. Observations

Observed data [*Saucier et al.*, 2004b] is from CTDs (Conductivity, Temperature and Depth measuring instruments) moored at eight different stations (see Fig. 1). Four stations are located in Hudson Bay, two are in Hudson Strait, and two are in southern Foxe Basin. All stations were occupied with CTDs for at least one year during August 2003–August 2006 (see Tab. 1 for the duration of the timeseries and the depth of the instruments). Pressure recorded every 30 min is used to study the seasonal modifications in the M_2 tide. We restrict our analyses to the M_2 wave since it dominates the tidal records and the currents in general [e.g., *Prinsenberg*, 1987].

The pressure record from each mooring is segmented into slightly overlapping monthly timeseries (32 days) for sequential harmonic analyses [*Mofjeld*, 1986; *Pawlowicz et al.*, 2002; *Foreman*, 1978]. This produces values for M_2 $\rho_s g\eta$ surface pressure and phase. The symbol ρ_s represents sea surface density and $g = 9.8$ m s^{-2}. The symbol η is the sea surface elevation above the mean sea level ζ. The sea surface elevation η and the mean sea level ζ include the submerged fraction of sea ice [see *Mellor and Kantha*, 1989, Fig. 1].

From the observations, the M_2 $\rho_s g\eta$ pressures typically deviate by 3×10^{-2} dbars from the annual mean. Such a large pressure deviation can hardly be related to changes in sea surface density (ρ_s). From observations at 25 m depth, and the model by *Saucier et al.* [2004a], monthly-averaged densities change by at most 2 kg m^{-3} over a year. For a tidal elevation with fixed amplitude $\eta = 1$ m, the resulting surface wave pressure change is $|\Delta(\rho_s g\eta)| = 2 \times 10^{-3}$ dbars, an order of magnitude smaller than the observed $\rho_s g\eta$ deviation. Thus, observed M_2 $\rho_s g\eta$ pressure amplitudes may be converted to η amplitudes without significant alteration. This is performed using a constant density value of $\rho_s = 1024\,\mathrm{kg\,m^{-3}}$ determined from available observations and model results [e.g., *Mofjeld*, 1986].

The pressure records used in this study were mostly obtained from CTDs located a few meters above sea floor, making them only slightly sensitive to a tilt of the mooring line. The shallowest instrument was located 35m below surface at station 4 in 2003 (Tab. 1). Records from this station are also available for years 2004 and 2005. The instruments in 2004 and 2005 were much deeper (7 m above sea floor) and the M_2 harmonics from 2004 and 2005 are consistent with those obtained from the shallow instrument in 2003. In any case, the software used for the harmonic analyses provides confidence intervals (level 95%) according to the spectrum of the residual, i.e. the energy that could not be related to tides [*Pawlowicz et al.*, 2002]. The intervals thus provide the error associated with the ambient noise.

One station in Hudson Strait was eliminated because of the poor quality of the pressure record. The mooring had only one CTD located close to the surface (at 30 m depth). Investigations have shown that the particularly strong currents found there caused a significant and irregular tilt of the mooring line [e.g., *Straneo and Saucier*, 2008]. Also, the seasonal variations of the phase of M_2 at station 25 are not available. Comparison between instrument records revealed that the internal clock of this particular CTD cumulated a lag of 10 hours over the year, which resulted in a gradual and artificial change in the phase of the wave over the months. Such lag was not observed in the records from the other instruments.

The measurements from a velocity profiler are also available for this study. This ADCP (Acoustic Doppler Current Profiler) was moored in a upward-looking position at station 7 from August 2003 to August 2004. The currents were recorded with a vertical separation of 2 m and a sampling frequency of 30 min. Harmonic analyses are performed over these velocity records to provide the seasonal variations of the M_2 velocity profile in the meridional direction. This corresponds to the amplitude of the horizontal M_2 currents in (approximately) the along-strait direction.

2.2. Numerical Simulations

The results from a numerical model [*Saucier et al.*, 2004a] are used to further investigate the M_2 variations. The model solves the 3–D hydrostatic primitive equations over the whole HBS domain (Foxe Basin, Hudson Bay/Strait, James and Ungava Bays, see Fig. 1). The horizontal resolution is 10 km and bathymetry is reproduced using 36 z-levels and partial cells at the bottom [e.g., *Adcroft et al.*, 1997]. The ocean model is coupled to a dynamic and thermodynamic two-layer sea ice model [*Hunke and Dukowicz*, 1997; *Semtner*, 1976], and a single layer snow model. Landfast ice is not included in the model. According to *Markham* [1986], landfast ice is important in only two locations, east of the Belcher Islands, and in northern Foxe Basin. The simulated ice velocities (Fig. 8a) are particularly small in these regions which is consistent with the behavior of landfast ice. The absence of landfast ice in the model should thus not represent an important limitation.

The simulation is conducted under realistic atmospheric, hydrologic, and oceanic forcing for the August 2003–August 2004 period. These forcing, initial salinity and temperature, momentum and scalar diffusion, and comparison with observations are discussed in *Saucier et al.* [2004a]. Tides are introduced by prescribing the sea elevation at open boundaries according to nine tidal constituents: M_2, S_2, N_2, K_2, O_1, K_1, P_1, M_4, and MS_4. These constituents are held constant throughout the simulation and astronomical forcing over HBS is neglected [see *Freeman and Murty*, 1976]. The free surface is treated using a semi-implicit time discretization and a 5 min timestep. Modeled harmonics are computed as with the observations but this time using modeled water levels sampled at the model timestep.

Table 2 shows a comparison between the simulated M_2 wave (Fig. 2) and observations. The largest relative errors are found in Roes Welcome Sound and in James Bay, and sensitivity experiments have shown that these errors can be attributed to the poorly constrained bathymetry of the basin. Significant variations in depths are visible when comparing common bathymetric databases and the nautical charts from the Canadian Hydrographic Service. The amplitude and phase in specific locations (Roes Welcome Sound, James Bay, and western Hudson Strait) were found particularly sensitive to changes in bathymetry, perhaps because of significant wave interference. The results from this study are obtained using Etopo2′v2 [*NOAA*, 2006] and the nautical charts from the Canadian Hydrographic Service.

The ocean currents and sea ice interact through a stress at the ice-ocean interface:

$$\boldsymbol{\tau}_{\mathrm{ice}} = \rho_0 C_{\mathrm{DIO}} \left\| \mathbf{v}_{\mathrm{water}} - \mathbf{v}_{\mathrm{ice}} \right\| (\mathbf{v}_{\mathrm{water}} - \mathbf{v}_{\mathrm{ice}}) \qquad (1)$$

where $\rho_0(\mathbf{x}_\mathrm{h})$ is time and depth-averaged seawater density, $\mathbf{x}_\mathrm{h}$ is the position in the horizontal (h) plane, C_{DIO} is the ice-ocean drag coefficient valid at five meters below ice ($z = -5$ m), $\mathbf{v}_{\mathrm{water}}(\mathbf{x}_\mathrm{h}, t)$ is the horizontal ocean velocity at $z = -5$ m, and $\mathbf{v}_{\mathrm{ice}}(\mathbf{x}_\mathrm{h}, t)$ is sea ice velocity. Empirically-derived ice-ocean quadratic drag coefficients are often calculated using ocean velocity at one meter below sea ice, and their magnitude is found in the range $1.32 \times 10^{-3} < C_{\mathrm{DIO}} < 26.8 \times 10^{-3}$ [*Langleben*, 1982; *Pease* *et al.*, 1983; *Madsen and Bruno*, 1986]. There is a considerable spread in these values as they were estimated in highly different ice conditions. For instance, *Steiner* [2001] suggests an empirical relation between ice thickness and the drag coefficient.

A series of experiments was conducted to determine the appropriate ice-ocean drag coefficient in the range $1\times10^{-3} < C_{\mathrm{DIO}} < 4\times10^{-3}$. The value 2×10^{-3} (applied at $z=-5$ m) produced satisfactorily agreement between observed and modeled M_2 surface elevations over the year. This value is close to that used by *Hibler* [1979] for the Arctic ice (5.5×10^{-3}). The spatial and temporal distributions of the friction under ice were found qualitatively similar in all our simulations. The main difference was that the simulations using the highest drag coefficients produced M_2 seasonal variations that exceeded the natural range shown by observations.

3. Results from Observations

The observed monthly variations of the M_2 surface elevation, referenced to the mean value in August, are shown for the four stations of Hudson Bay in Fig. 3a. Significant elevation decrease is seen at station 7 from August to October. The decrease is also seen at stations 6 and 2, although it is not significant at the 95% level. Following this late summer decrease, amplitudes rise abruptly in December. The December rise is significant for stations 6 and 2 while station 7 shows a similar but non significant change. Winter (January to March) is characterized by decreasing amplitudes that are significant at all stations. During spring (April to July), amplitudes gradually rise back to their August value. The M_2 variability at these stations is similar to that from *Godin* [1986] and *Prinsenberg* [1988].

Figure 3b shows the monthly variations of the M_2 surface elevation in Hudson Strait and Foxe Basin. The late summer/early autumn amplitude decrease is found again in Hudson Strait and Foxe Basin, and is significant at all stations. The December abrupt amplitude rise found in Hudson Bay can be compared to a similar rise occurring over January in Hudson Strait and Foxe Basin. During winter, stations 8 and 25 show a significant amplitude decrease also followed by a gradual increase back up to their August value. Recall that stations 8 and 25 are located in southern Foxe Basin, and stations 9 and 10 in western Hudson Strait (see Fig. 1). Stations 9 and 10 show a significant amplitude increase during winter and spring (January–May), with levels above those found in August.

The phase of the tidal wave also fluctuates over the year. Figure 4a shows these fluctuations for the stations inside Hudson Bay. A significant seasonal cycle is seen at all stations except station 4. The phase is advanced (high and low tides occur earlier) and the largest deviations are found during March and April. This deviation is particularly large at station 2 as the M_2 tide is earlier by 30 min ($-14°$). Figure 4b shows the fluctuations of the wave in Hudson Strait and Foxe Basin. The deviations are much smaller than in Hudson Bay and do not exceed $\pm2°$. A significant seasonal cycle occurs at all stations with maximum deviations also around March and April. The phase is advanced at station 9 (mouth of Hudson Bay) but it is retarded in Foxe Basin and western Hudson Strait (stations 8 and 10, respectively). The phase at station 25 is not available (see §2).

Multiyear timeseries are available at two stations and similar seasonal variations are observed over the years. Figure 5 shows the two longest timeseries available (3 years at station 4, and 2 years at station 2). A minimum is found over February–March of each year with small but significant interannual variations. The most noticeable anomaly is seen in June 2004. The figure also shows the variations of the phase at these stations. The particularly large deviation at station 2 is observed during the two sampled years.

The wave amplitudes that were shown in Figs. 3 and 5a represent the divergence $\boldsymbol{\nabla}\cdot\overline{\mathbf{v}}$ of the depth-averaged current $\overline{\mathbf{v}}$. These values only reflect the vertical integration of all the changes in the tidal velocity profile. The velocity profile was measured at station 7 over the Aug. 2003–Aug. 2004 period, and Fig. 6a shows the meridional (i.e. approximately along-strait) amplitude of the M_2 velocities. The seasonal variations mainly occur in the first 30 m below the surface and the largest deviation from summertime values (Aug.–Sep.) occurs during the Feb.–March period. Note the increasing velocities at 80 m as the surface velocities decrease. These results are consistent with those from Fig. 3a and support the hypothesis of a seasonal modulation of tides caused by under-ice friction.

The new observations revealed three previously unknown features of the M_2 seasonal variability. First, significant variations occur all over the year and not only during winter. Then, the variability in Hudson Strait is qualitatively different from the one in Hudson Bay and Foxe Basin. Finally, the M_2 seasonal variations were found to be reproducible and similar over the years. The nature of this complex M_2 variability will be examined in the next section (§4) with the help of numerical experiments.

4. Results from Numerical Experiments

The complex M_2 variability depicted in Figs. 3a,b and 4a,b is now examined using a numerical model. The model is able to simulate complete seasonal cycles of tidal amplitude and phase, and qualitatively reproduce most of the features of the observed variability. We first present a comparison between the modeled and observed variability. Then, we conduct an experiment where the ice-ocean stress is removed, in order to determine its role in the seasonal variations. The remote effect of the ice-ocean stress upon tides is presented. Finally, some effects of the tides upon the sea ice cover are introduced.

4.1. Comparison with Observations

Figures 3c,d and 4c,d show modeled results that correspond to the same period (Aug. 2003–Aug. 2004) and locations as the observations shown above. The model reproduces well the temporal variability of the variations, including summer decrease, the December abrupt rise in amplitude, largest deviations in amplitude and phase occurring in March, the relatively large phase deviation at station 2, and the general return to summertime values in July. However, the model overestimates or underestimates the variations at some stations, and does not reproduce the phase advance at stations 7 and 9. Investigations have shown that these errors can be related to the uncertain bathymetry in some locations (see §2).

Regarding the effect of the ice-ocean friction upon the tidal velocity profiles, Fig. 6 shows a comparison between observed and modeled results at station 7. The modeled velocities show a constant barotropic overestimation of approximately 15 cm s^{-1}, an error already visible in Tab. 2 and that can be related to errors in bathymetry (see §2). Apart from this constant barotropic offset, it can be seen that the model satisfactorily represents the seasonal variations, including thickness of the surface boundary layer, magnitude of the seasonal deviations in the upper velocities, and timing of the seasonal changes (minimum velocities over Feb.–March).

4.2. The Role of the Ice-Ocean Friction in the Modification of Tides

The modeled results presented so far (Tab. 2, Figs. 3c,d, 4c,d, and 6b) were obtained from a simulation using realistic conditions and this simulation will be called the control simulation hereafter. The presumed influence of under-ice friction upon the M_2 variability will now be discussed using the results of a second simulation with the same conditions as in the control, except that the ice-ocean friction is removed. Thus the dynamics remains the same in the ice-free situation but the tides are no longer damped by friction underneath the ice.

The comparison between the control (Fig. 3c,d) and the no-ice-ocean stress simulation (Fig. 3e,f) shows that the late summer decrease (first noticed in observations, Fig. 3a,b) is not modified by removing the ice-ocean stress. However, the M_2 variations during winter are greatly diminished by removing the ice-ocean stress. The stress causes a winter elevation decrease in Hudson Bay and Foxe Basin, and a small increase in western Hudson Strait (station 9). A similar comparison for the phase of the control (Fig. 4c,d) and the no-ice-ocean stress simulation (Fig. 4e,f) shows that the seasonal phase variations essentially vanish when the ice-ocean stress is removed.

Significant variance remains after the removal of the ice-ocean stress (Fig. 3e,f). The comparison of these curves with those observed (Fig. 3a,b) suggests that the remaining oscillations also occur in reality (but are partly obscured by the ice-ocean friction). For instance, a decrease is visible from July to November at stations 7, 6, 8, 25, 9 and 10, and an abrupt increase is visible in Dec.–Jan. at stations 7, 6, 8 and 25. The model seems to qualitatively reproduce these oscillations but their cause remains unknown.

4.3. Local and Remote Effects of the Ice-Ocean Stress upon Tides

The results from §4.2 have shown that the effect of the ice-ocean friction is generally important for the phase or the amplitude of the M_2 wave. However, significant regional differences are noticeable in both observed and modeled seasonal variations. In this section, we examine these regional differences using the results from the numerical model.

Figure 7 shows the modification of the wave during the month when the ice cover is maximum (March). The amplitude of the wave increases in some locations and such increase is also visible in the observations from stations 9 and 10. The model predicts a significant decrease in eastern Hudson Bay and James Bay (consistent with the observations from *Godin* 1986) but the decrease in western Hudson Bay is known from Fig. 3a,c to be excessive. The modification of the phase is particularly important in northeastern Hudson Bay, a prediction that is consistent with the observations from station 2.

These changes were shown in §4.2 to be essentially caused by the friction under ice. However, we don't know if this friction acts all over the system or if it is concentrated in specific locations. To answer this question, the rate at which the ice-ocean friction removes the barotropic energy at a given location is quantified for the month of March 2004 using Eq. 2:

$$D_{\mathrm{ice}} = \overline{\mathbf{v}} \cdot \boldsymbol{\tau}_{\mathrm{ice}} c \tag{2}$$

In this equation, $\overline{\mathbf{v}}(\mathbf{x}_{\mathrm{h}}, t)$ is the depth-averaged horizontal (h) ocean velocity, $\boldsymbol{\tau}_{\mathrm{ice}}$ is described in Eq. 1, and $0 < c < 1$ is the local ice concentration. The result from this computation, averaged over 708 h (approximately one month), is shown in Fig. 8b. The magnitudes vary largely because of the cubic relation with water velocity, i.e. $D_{\mathrm{ice}} \propto \overline{\mathbf{v}} \cdot \|\mathbf{v}_{\mathrm{water}} - \mathbf{v}_{\mathrm{ice}}\| (\mathbf{v}_{\mathrm{water}} - \mathbf{v}_{\mathrm{ice}})$. The dissipation is concentrated along coasts, over shallow regions such as James Bay and eastern Foxe Basin, and where the amplitude of the wave is large (see Fig. 2a). The domain-integrated rate of dissipation averaged over March 2004 is 40 GW, which represents 18% of the dissipation that occurs over the sea floor during the same period (220 GW).

These results show that the changes in Fig. 7 are caused by friction that mostly occurs in Foxe Basin. The effects of the friction are however visible in remote locations (far from Foxe Basin) since friction leads to a modification of the interference pattern over the whole system. For instance, the large phase deviation at station 2 is, according to the model, caused by the shoreward displacement of the nearby amphidromic point during winter (the point is visible in northeastern Hudson Bay, Fig. 2b). This particular amphidromic point becomes degenerate [e.g., *Pugh*, 1987, p. 261] during winter because of friction.

4.4. The Effects of the Tides upon the Ice Cover

The previous sections focused on the effects of the ice-ocean friction upon the M_2 wave. We will conclude this study by showing some effects of the tides upon the ice cover according to the control simulation. Figure 8a shows the ellipses of tidal ice drift for the M_2 wave during the month of maximum ice cover (March 2004). It is found that significant ice movements are induced by the tides. The ice velocities are approximately 30 cm s^{-1} in Hudson Strait and Foxe Basin but attain 1 m s^{-1} in southeastern Foxe Basin (the M_2 tidal range is above 4 m in these locations). Lower velocities (below 15 cm s^{-1}) are found in the other regions. The ice ellipses are similar to those of the M_2 barotropic tide (not shown) except that the ice velocities are generally lower. Notably, the ratio between the barotropic M_2 velocities and the ice velocities exceeds 3 in northern Foxe Basin, James Bay, and southeastern Hudson Bay.

The low ice velocities in southeastern Hudson Bay and northern Foxe Basin are consistent with the recurrent presence of landfast ice in these areas [*Markham*, 1986] but further work would be required to understand this uneven response to tides, and the effect of tides upon ice mechanics. For instance, tidally-induced movements of ice may contribute to the redistribution (ridging) and deformation of the ice cover. The modeled internal ice stress components σ_{11} and σ_{22} (σ is the internal ice stress tensor, see *Hunke and Dukowicz* 1997) essentially oscillate at a semidiurnal rate, and Fig. 9 provides the peak-to-peak amplitude of the internal ice stress $\sqrt{\sigma_{11}^2 + \sigma_{22}^2}$ oscillation at M_2 frequency, along with the thickness of the ice cover during March 2004. It is seen that the tidally-induced ice stress is most important in Foxe Basin, with values of the same order of magnitude as semidiurnal fluctuations observed in the Barents Sea (25 to 50 kPa) [*Tucker and Perovich*, 1992].

5. Discussion

The seasonal variability of the M_2 elevation was examined using new observations from Hudson Bay, Hudson Strait, and Foxe Basin. It was shown for the first time that significant seasonal M_2 variability occurs throughout the system and at all seasons. This expands the results from *Godin* [1986] and *Prinsenberg* [1988] as their studies were limited to Hudson Bay and James Bay. Another new result is the presence of variations in the tidal wave during the ice-free period. Although these variations were qualitatively captured by the model, their cause remains unknown.

The largest fluctuations occur during winter and are qualitatively different amongst regions. The M_2 elevation in Hudson Bay and Foxe Basin decreases from December to March, but the elevation in Hudson Strait increases. Such increase was also observed in the Bering Sea by *Mofjeld* [1986] but the cause of these variations could not be determined. Our numerical experiments confirm that the winter modifications of the M_2 elevation in HBS are essentially caused by the under-ice stress, as suspected by *Godin* [1986]. These experiments also show that the friction is mostly active in a limited region (Foxe Basin) and modifies the position of the amphidromic points in remote locations (station 2).

6. Conclusions

Significant seasonal changes in M_2 elevations are found in all the regions of the Hudson Bay System, and at all seasons. The largest changes occur during winter while both elevation increase (Hudson Strait) and decrease (Hudson Bay, Foxe Basin) are observed. These variations are found recurrent at the stations where multiyear observations are available. Numerical simulations show that the winter M_2 variations are essentially caused by the under-ice friction. This friction mostly occurs in a limited region (Foxe Basin) and can account for both the increased and decreased elevations during winter.

Acknowledgments.
The authors would like to thank the Department of Fisheries and Oceans, the captains and crews of the CCGS Pierre Radisson and Des Groseillers, technicians Sylvain Cantin, Roger Pigeon, Rémi Desmarais and Simon Senneville. The authors would also like to thank J. Caveen and F. Roy for technical support. We gratefully thank Fiamma Straneo and two anonymous reviewers for helpful comments and suggestions which led to the improvement of this paper. We thank the Natural Sciences and Engineering Research Council of Canada, and the Canadian Foundation for Climate and Atmospheric Sciences. This is a contribution to the Canadian CLIVAR and ArcticNet programs.

References

Adcroft, A., C. Hill, and J. Marshall (1997), Representation of topography by shaved cells in a height coordinate ocean model, *Mon. Weather Rev.*, *125*(9), 2293–2315.

Foreman, M. (1978), Manual for tidal currents analysis and prediction, *Tech. rep.*, Inst. Ocean Sci., Patricia Bay, Sidney, B.C. (Canada).

Freeman, N., and T. Murty (1976), Numerical modeling of tides in Hudson Bay., *J. Fish. Res. Board Can.*, *33*(10), 2345–2361.

Godin, G. (1986), Modification by an ice cover of the tide in James Bay and Hudson Bay, *Arctic*, *39*(1), 65–67.

Godin, G., and F. Barber (1980), Variability of the tide at some sites in the Canadian Arctic, *Arctic*, *33*, 30–37.

Heil, P., J. Hutchings, A. Worby, M. Johansson, J. Launiainen, C. Haas, and W. Hibler, III (2008), Tidal forcing on sea-ice drift and deformation in the western Weddell Sea in early austral summer, 2004, *Deep-Sea Res. II*, *55*, 943–962, doi:10.1016/j.dsr2.2007.12.026.

Hibler, W., III (1979), A dynamic thermodynamic sea ice model, *J. Phys. Oceanogr.*, *9*, 815–846.

Holloway, G., and A. Proshutinsky (2007), Role of tides in Arctic ocean/ice climate, *J. Geophys. Res.*, *112*, C04S06, doi:10.1029/2006JC003643.

Hunke, E., and J. Dukowicz (1997), An elastic-viscous-plastic model for sea ice dynamics, *J. Phys. Oceanogr.*, *27*(9), 1849–1867.

Johnson, W., and Z. Kowalik (1986), Modeling of storm surges in the Bering Sea and Norton Sound, *J. Geophys. Res.*, *91*(C4), 5119–5128.

Kagan, B., D. Romanenkov, and E. So Ana (2008), Tidal ice drift and ice-generated changes in the tidal dynamics/energetics on the Siberian continental shelf, *Cont. Shelf Res.*, *28*, 351–368, doi:10.1016/j.csr.2007.09.004.

Langleben, M. (1982), Water drag coefficient of first-year sea ice, *J. Geophys. Res.*, *87*(C1), 573–578.

Madsen, O., and M. Bruno (1986), A methodology for the determination of drag coefficients for ice floes, in *Proceedings of the Fifth international offshore mechanics and Arctic engineering symposium*, vol. 4, pp. 410–417, Am. Soc. Mech. Eng.

Markham, W. (1986), The ice cover, in *Canadian Inland Seas*, edited by I. Martini, pp. 101–116, Elsevier oceanogr. series.

Martin, S., I. Polyakov, T. Markus, and R. Drucker (2004), Okhotsk Sea Kashevarov Bank polynya: Its dependence on diurnal and fortnightly tides and its initial formation, *J. Geophys. Res.*, *109*(C09S04), 16, doi:10.1029/2003JC002215.

Mellor, G., and L. Kantha (1989), An ice-ocean coupled model, *J. Geophys. Res.*, *94*(C8), 10,937–10,954.

Mofjeld, H. (1986), Observed tides on the Northeastern Bering Sea Shelf, *J. Geophys. Res.*, *91*(C2), 2593–2606.

Murty, T. (1985), Modifications of hydrographic characteristics, tides, and normal modes by ice cover, *Mar. Geod.*, *9*(4), 451–468.

NOAA (2006), 2-minute gridded global relief data (Etopo2v2), *Tech. rep.*, U.S. Department of Commerce, National Geophysical Data Center.

Pawlowicz, R., B. Beardsley, and S. Lentz (2002), Classical tidal harmonic analysis including error estimates in Matlab using T-Tide, *Comput. Geosci.*, *28*(8), 929–937.

Pease, C., S. Salo, and J. Overland (1983), Drag measurements for first-year sea ice over a shallow sea, *J. Geophys. Res.*, *88*, 2053–2862.

Polyakov, I., and S. Martin (2000), Interaction of the Okhotsk Sea diurnal tides with the Kashevarov Bank polynya, *J. Geophys. Res.*, *105*(C2), 3281–3294.

Prinsenberg, S. (1987), Seasonal current variations observed in western Hudson Bay, *J. Geophys. Res.*, *92*(C10), 10,756–766.

Prinsenberg, S. (1988), Damping and phase advance of the tide in western Hudson Bay by the annual ice cover., *J. Phys. Oceanogr.*, *18*(11), 1744–1751.

Prinsenberg, S., and J. Hamilton (2005), Monitoring the volume, freshwater and heat fluxes passing through Lancaster Sound in the Canadian Arctic Archipelago, *Atmos.-Ocean*, *43*(1), 1–22.

Pugh, D. (1987), *Tides, surges and mean sea-level*, J. Wiley Chichester.

Saucier, F., S. Senneville, S. Prinsenberg, F. Roy, G. Smith, P. Gachon, D. Caya, and R. Laprise (2004a), Modelling the sea ice-ocean seasonal cycle in Hudson Bay, Foxe Basin and Hudson Strait, Canada, *Clim. Dyn.*, *23*(3-4), 303–326, doi:10.1007/s00382-004-0445-6.

Saucier, F., M. Starr, M. Harvey, and J. Therriault (2004b), Expédition MERICA 2003: Suivi et étude du climat et de la productivité de la baie d'Hudson, *Nat. Can.*, *128*, 108–110.

Semtner, A. (1976), A model for the thermodynamic growth of sea ice in numerical investigations of climate, *J. Phys. Oceanogr.*, *6*, 379–389.

Steiner, N. (2001), Introduction of variable drag coefficients into sea-ice models, *Ann. Glaciol.*, *33*, 181–186.

Straneo, F., and F. Saucier (2008), The outflow from Hudson Strait and its contribution to the Labrador Current, *Deep Sea-Res. I*, *55*(8), 926–946, doi:10.1016/j.dsr.2008.03.012.

Sverdrup, H. (1927), Dynamics of tides on the North Siberian Shelf, *Geofys. Publ.*, *4*, 75.

Tucker, W., III, and D. Perovich (1992), Stress measurements in drifting pack ice, *Cold Regions Science and Technology*, *20*, 119–139.

Zubov, N. (1943), *Arctic ice*, 491 pp., Izdatel'stvo Glavsermorputi, Moscow, trans. U.S. Navy Electronics Laboratory (1963).

P. St-Laurent, Institut des Sciences de la Mer, Université du Québec à Rimouski, 310 des Ursulines, Rimouski, QC, G5L 3A1, Canada. (Pierre.St-Laurent@uqar.qc.ca)

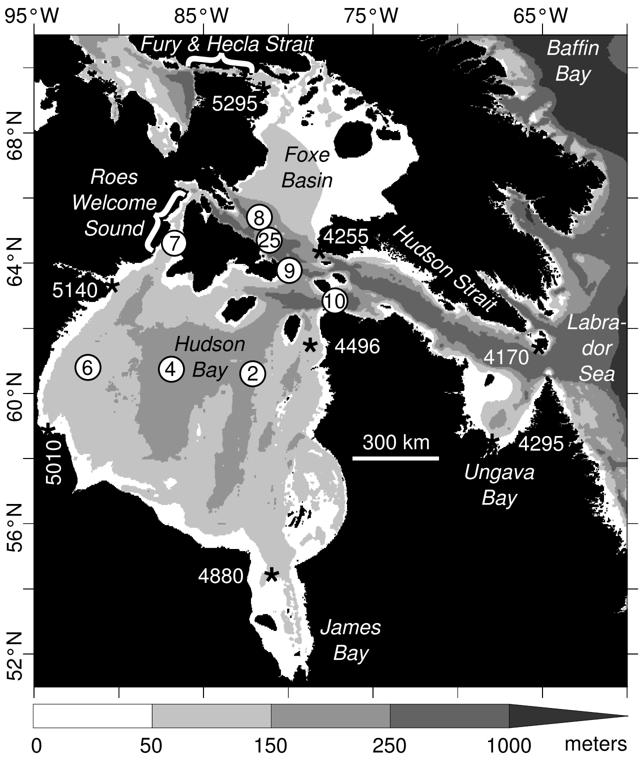

Figure 1. Map of the Hudson Bay System (HBS: Hudson Bay, Hudson Strait, Foxe Basin, James Bay, and Ungava Bay) with neighboring Labrador Sea and Baffin Bay. The stations used for the seasonal analyses are indicated by circled numbers. The stations used in Tab. 2 are indicated as black stars.

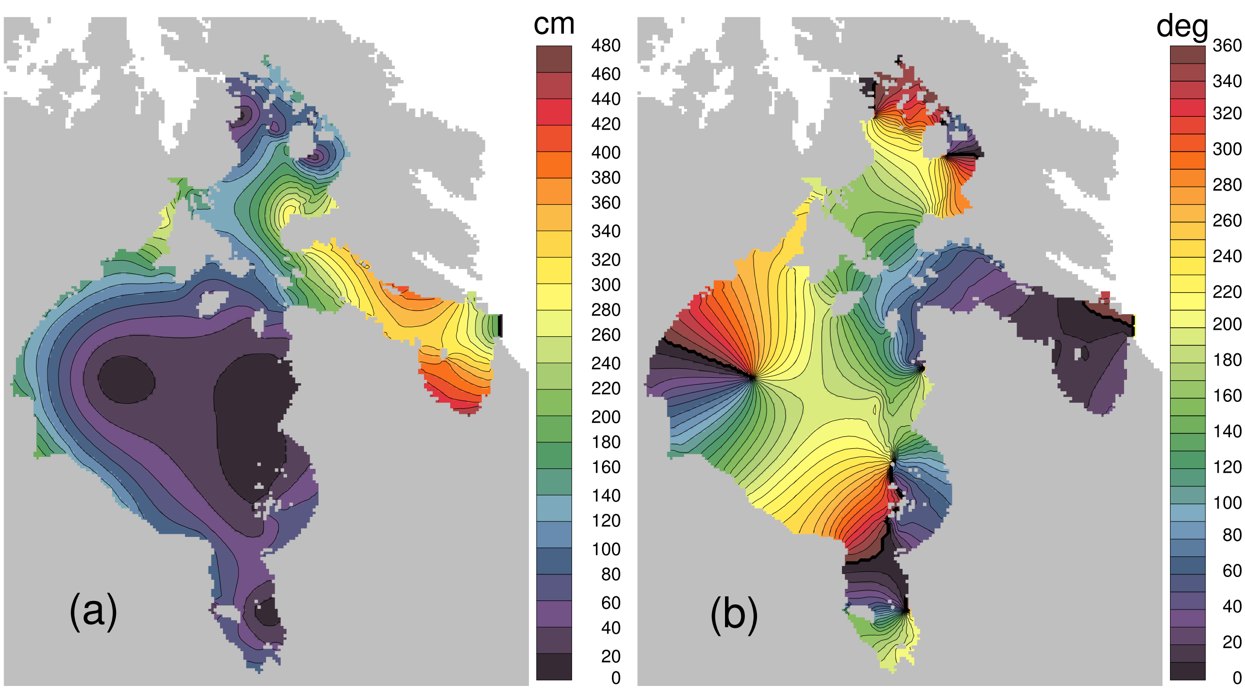

Figure 2. (a) Amplitude and (b) phase (relative to Greenwich) of the M_2 surface tidal wave during September 2003 (ice-free period) in the control simulation.

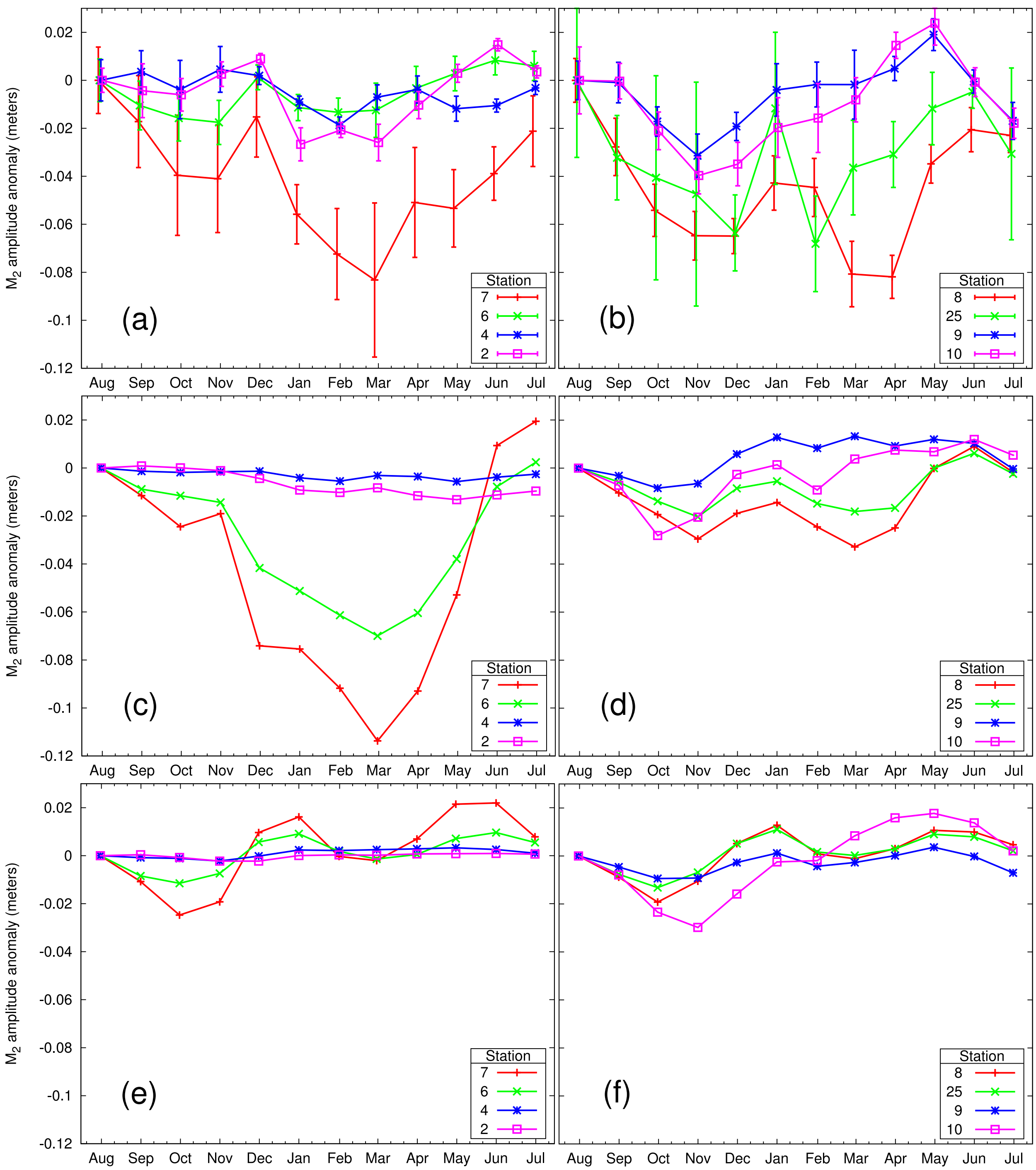

Figure 3. Monthly elevation of the surface M_2 tidal wave from (a,b) observations, (c,d) the control simulation, and (e,f) the experiment without ice-ocean stress. All values are referenced to those in August.

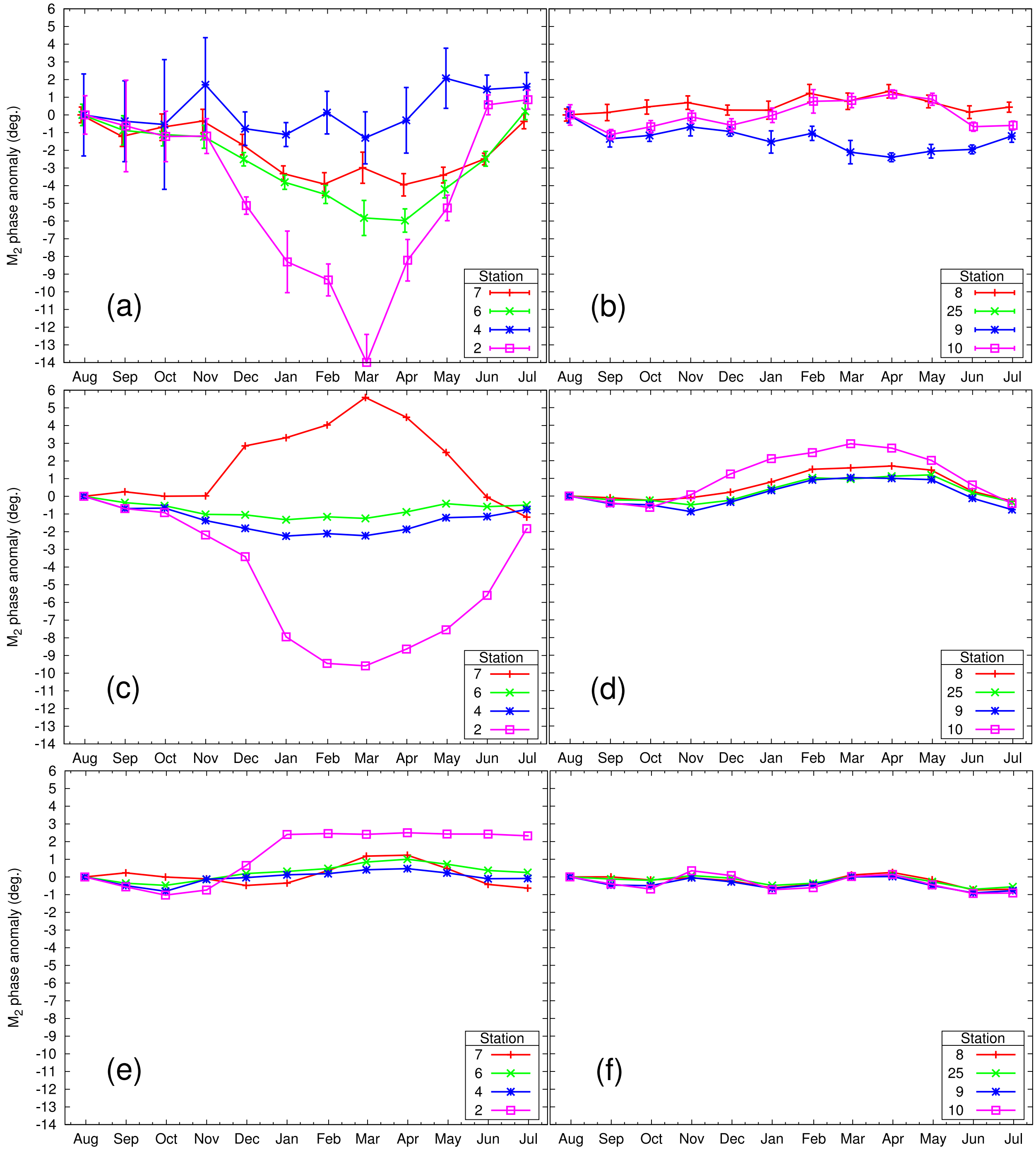

Figure 4. Monthly phase of the surface M_2 tidal wave from (a,b) observations, (c,d) the control simulation, and (e,f) the experiment without ice-ocean stress. All values are referenced to those in August. No observations are available for the phase at station 25 (see text).

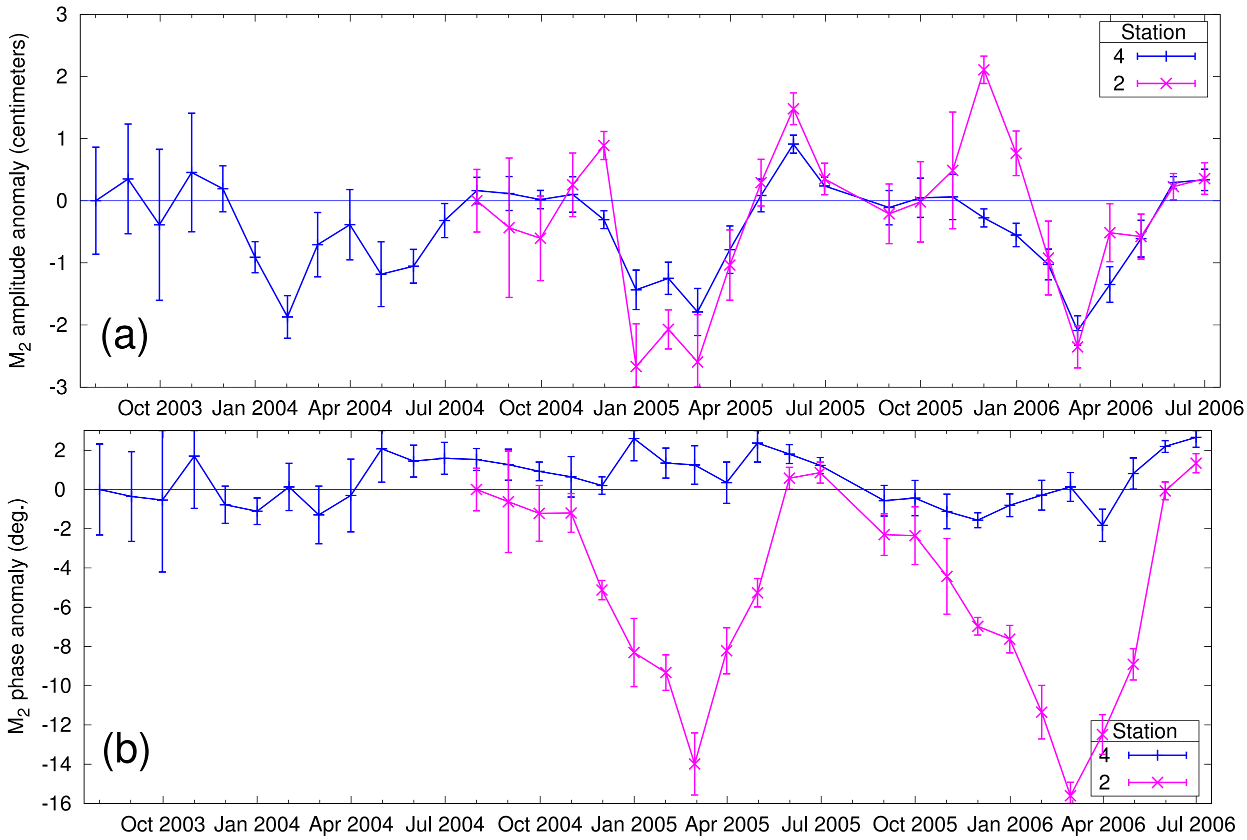

Figure 5. Multiyear timeseries of (a) amplitude and (b) phase of the M_2 surface wave from observations. The values at station 4 (2) are referenced to those in August 2003 (2004).

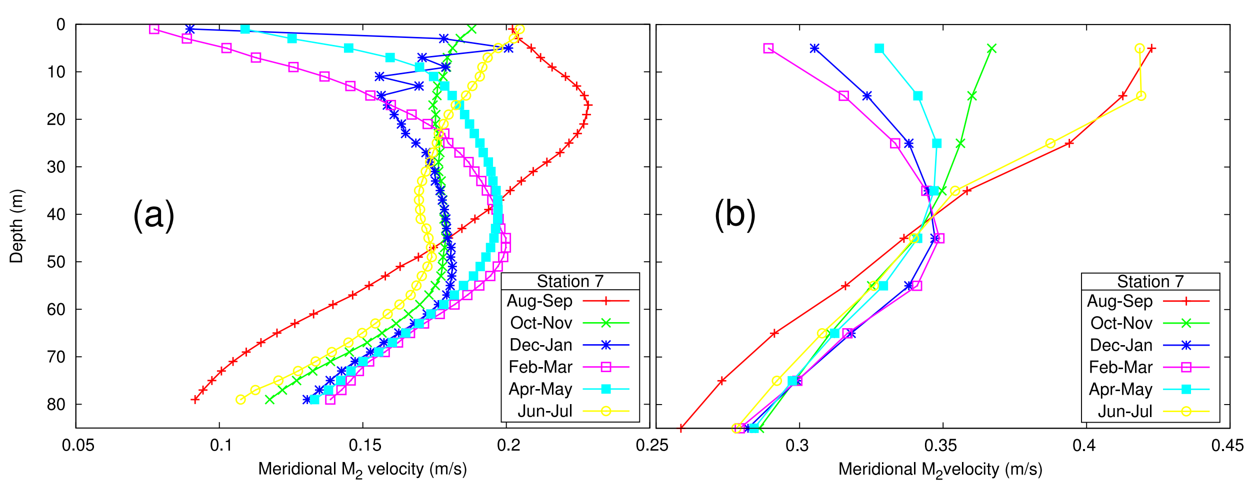

Figure 6. Meridional M_2 velocity profile at station 7 from (a) observations and (b) the control simulation for the 2003–2004 period.

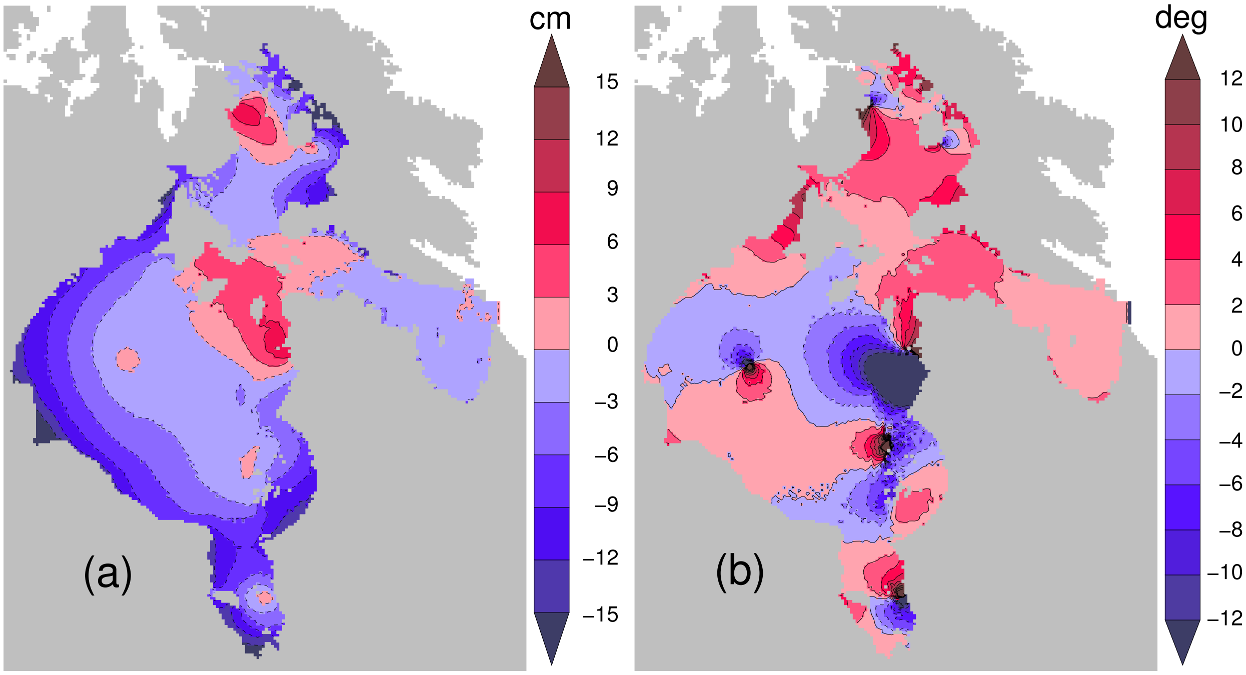

Figure 7. (a) Amplitude anomaly $A_{\text{March}} - A_{\text{Sept}}$ and (b) phase anomaly $\phi_{\text{March}} - \phi_{\text{Sept}}$ for the M_2 surface tidal wave in the control simulation. September is a generally ice-free period and March is the month of maximum ice cover.

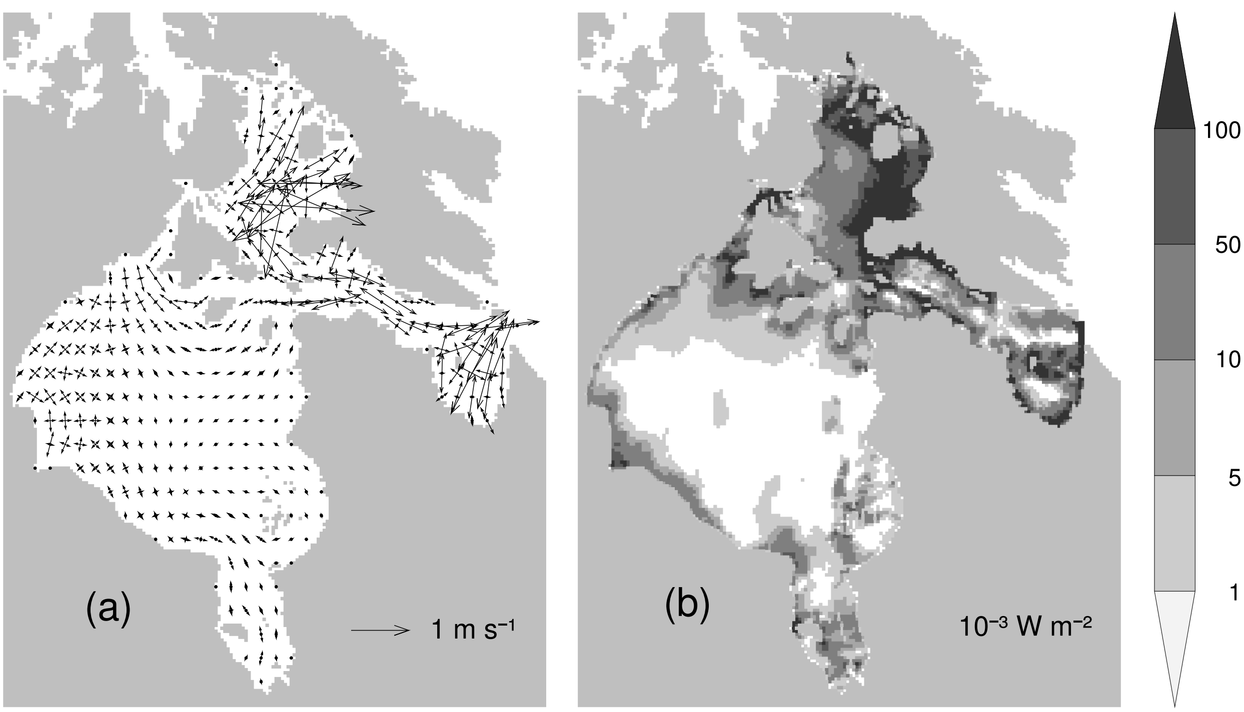

Figure 8. (a) Ellipses of tidal ice drift for the M_2 wave and (b) under-ice barotropic energy dissipation rate during the month of March 2004 (maximum ice cover) in the control simulation.

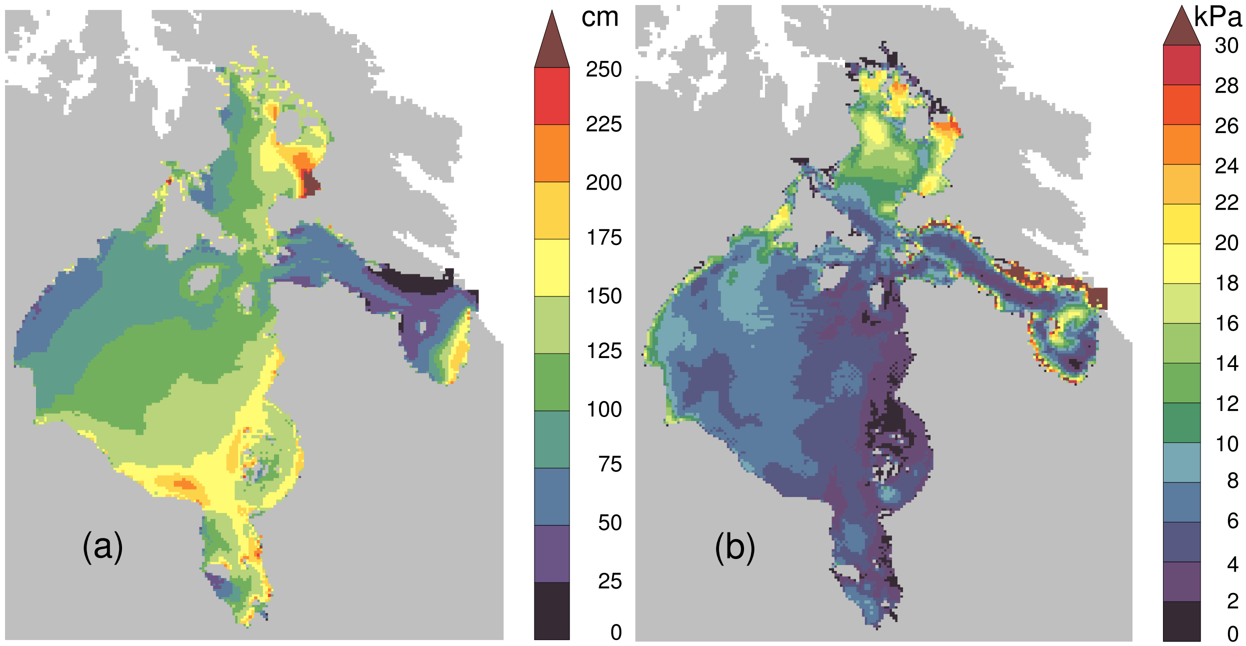

Figure 9. (a) Average thickness of sea ice during March 2004 from the control simulation. (b) Peak-to-peak amplitude of the internal ice stress $\sqrt{\sigma_{11}^2 + \sigma_{22}^2}$ oscillation at the M_2 frequency during March 2004 (control simulation).

Table 1. Location, period and depth of the pressure records used in the study. All timeseries begin in August of the indicated year and last one year. *H* is the depth of the water column.

Station	2003	2004	2005	Depth (m)	*H* (m)
2[a]		X	X	148	155
4[b]	X	X	X	35	205
6	X			63	108
7	X			100	103
8	X			440	443
9	X			149	152
10	X			374	377
25		X		363	366

[a] The 2004 timeseries is used in Fig. 3.
[b] The 2003 timeseries is used in Fig. 3.

Table 2. Comparison between observed (o) and modeled (m) values for the M_2 surface elevation amplitude A and phase ϕ relative to Greenwich. No observations are available for the phase at station 25 (see text).

Station	A_o (m)	ϕ_o (deg)	$A_m - A_o$ (m)	$\phi_m - \phi_o$ (deg)
4170	2.3	349	0.22	8
4255	2.1	112	−0.08	−7
4295	4.1	14	0.35	8
4496	0.4	95	−0.04	−24
4880	1.0	4	−0.38	2
5010	1.5	26	0.19	10
5140	1.4	276	0.14	−9
5295	0.7	0	−0.04	1
2	0.26	171	−0.07	1
4	0.18	243	0.02	0
6	0.74	335	0.04	3
7	1.78	258	0.47	−10
8	1.40	160	−0.02	−6
9	1.08	116	0.03	−16
10	1.31	59	0.37	3
25	1.30	na	−0.09	na